AMERICAN SOCIETY of
GENE & CELL THERAPY

In Vivo Imaging of Oncolytic Measles Virus Propagation with Single-Cell Resolution

Iris Kemler,[1] Matthew K. Ennis,[1] Claudia M. Neuhauser,[2] and David Dingli[1,3]

[1]Department of Molecular Medicine, Mayo Clinic, Rochester, MN 55905, USA; [2]Department of Mathematics, University of Houston, TX 77204, USA; [3]Division of Hematology, Department of Internal Medicine, Mayo Clinic, Rochester, MN 55905, USA

Recombinant measles viruses (MVs) have oncolytic activity against a variety of human cancers. However, their kinetics of spread within tumors has been unexplored. We established an intravital imaging system using the dorsal skin fold chamber, which allows for serial, non-invasive imaging of tumor cells and replication of a fusogenic and a hypofusogenic MV. Hypofusogenic virus-infected cells were detected at the earliest 3 days post-infection (dpi), with peak infection around 6 dpi. In contrast, the fusogenic virus replicated faster: infected cells were detectable 1 dpi and cells were killed quickly. Infection foci were significantly larger with the fusogenic virus. Both viruses formed syncytia. The spatial relationships between cells have a major influence on the outcome of therapy with oncolytic viruses.

INTRODUCTION

The use of replication-competent viruses to eliminate tumors (oncolytic virotherapy) is a novel and unique cancer therapy that is showing promising results. Viruses from several families are currently being evaluated in clinical trials.[1,2] Over the years, viruses have evolved or have been engineered to selectively infect and replicate in tumor cell populations, leading to cancer cell death via different mechanisms, including direct cell lysis or by the induction of cell-to-cell fusion[3] or immune system activation.[1,2,4] Moreover, viruses may be armed with recombinant genes to enhance their oncolytic activity, including a bystander effect.[1,2] Recently it was reported that a single, systemic injection of an engineered oncolytic measles virus (measles virus-sodium iodide symporter [MV-NIS][5]) led to a complete and durable (>3-year) remission in a patient with disseminated, relapsed, and refractory multiple myeloma.[6] Unfortunately, other patients receiving similar treatment did not have such a favorable outcome.[7] The reasons behind these disparate results are unclear. The dynamics of spread of such viruses in tumors has been largely unexplored. The perception has been that MV spreads slowly through the tumor compared to other oncolytic viruses, such as adenovirus or vesicular stomatitis virus.[8] Given that the outcome of tumor virotherapy depends on the race among the tumor, virus, and immune system,[9] it is critical to understand the dynamic interactions among the tumor, oncolytic virus, local microenvironment, and immune response.

Tumor therapy with replicating oncolytic viruses is an exercise in population dynamics, and mathematical models have been developed to understand and predict outcomes of therapy.[10–13] However, most mathematical models are only indirectly based on *in vivo* studies, since population sizes are usually inferred and not directly measured. The development of such models that faithfully reproduce the *in vivo* dynamics can be greatly facilitated by technologies that enable the serial and non-invasive quantitation in real time of the tumor and virus-infected cell populations at high resolution. To this end, viruses have been engineered to encode transgenes that track viral replication by various *in vivo* imaging methods, e.g., luciferase (bioluminescence), thymidine kinase, and the NIS gene (radioactivity and micro computed tomography/single-photon emission computed tomography [microCT/SPECT]).[14] Unfortunately, these imaging techniques have limited spatial resolution (1–2 mm for bioluminescence and 0.25 mm for microCT/SPECT), and they are, therefore, restricted to the macroscopic scale of organs. In contrast, multi-photon imaging with fluorophores allows for subcellular resolution, and, in addition, it has deep tissue penetration as well as reduced phototoxicity and photobleaching.[15–17] When combined with serial, non-invasive imaging in live animals (intravital microscopy), the infection kinetics can be analyzed and quantitated over a time span of several days at a cellular level. The approach may highlight current barriers to the spread of oncolytic viruses and perhaps enable improvements in vector design and clinical protocols.

To properly understand the dynamics of virotherapy and inform the development of mathematical models that can help optimize therapy,[18] we have established an intravital imaging system using the dorsal skin fold chamber (DSFC), a widely used *in vivo* model for preclinical cancer research.[19–24] We generated HT1080 tumor cells (human fibrosarcoma) expressing either tdTomato or the EGFP fluorophore. We also engineered replication-competent MV (Edmonston vaccine lineage) to express the enhanced blue fluorescent protein (EBFP2) with a nuclear localization sequence (NLS), such that every MV-infected cell accumulates EBFP exclusively in the nucleus. This clearly distinguishes one infected cell from the next one and enables easy detection and quantification of infected tumor cells. Viruses were used to infect fluorescent tumor cells in the DSFC, and virus
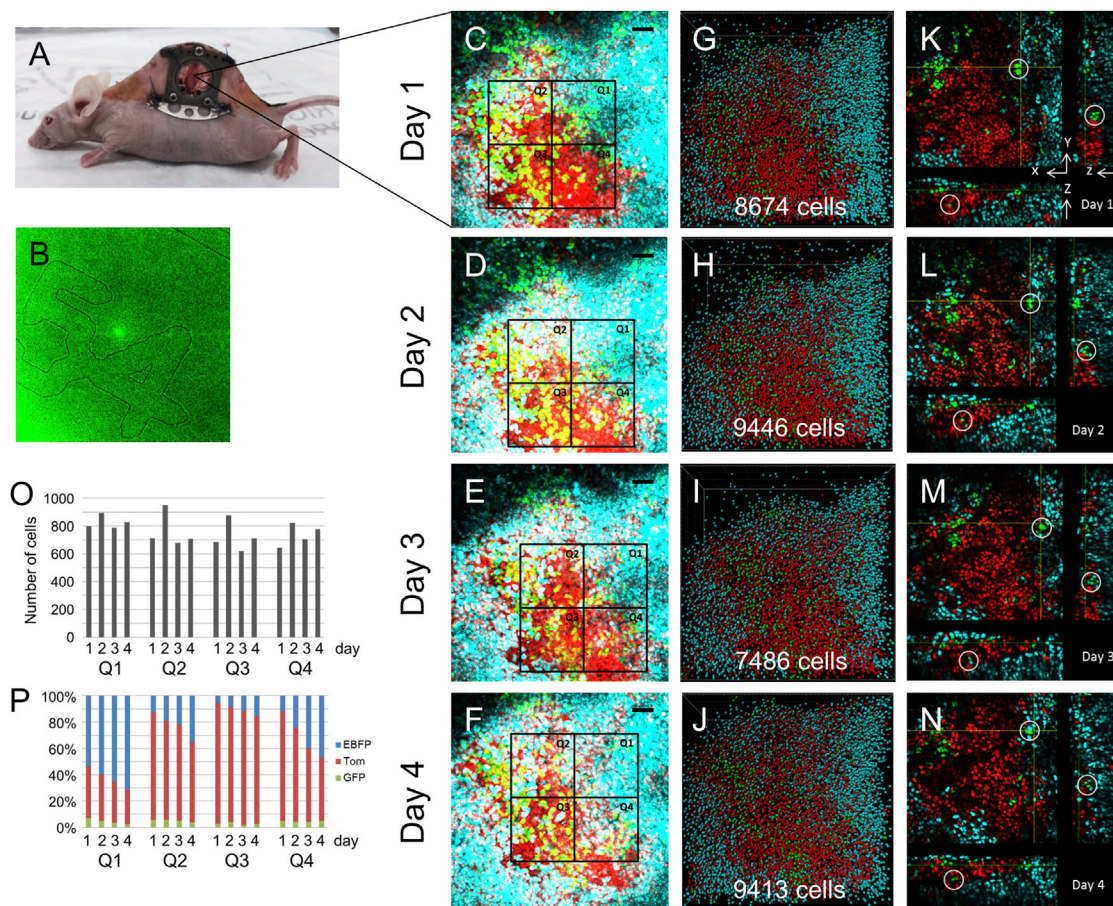
Figure 1. Serial Intravital Imaging of Multicolored HT1080 Tumor Cells

(A) NCR athymic nude mouse with a dorsal skin fold chamber (DSFC) implanted. (B) To retrace areas of interest over several days of imaging, a gridded coverslip was inserted and its numbers were visualized by reflectance imaging. (C–F) Maximum-intensity projections of HT1080-tdTomato-nuclear localization sequence (NLS), HT1080-EGFP-NLS, and HT1080-EBFP-NLS tumors imaged on day 1 (C), day 2 (D), day 3 (E), and day 4 (F). Outline of Q1–Q4 used to analyze cell numbers is shown. Scale bars, 50 µm. (G–J) The number of tumor cells was determined with the Imaris spot analysis software on day 1 (G), day 2 (H), day 3 (I), and day 4 (J). (K–N) Individual 2D slice and xz and yz orthogonal views of a z stack of tumor imaged on day 1 (K), day 2 (L), day 3 (M), and day 4 (N). White circles mark GFP cell clusters used as reference points to place Q1–Q4. (O) Total cell numbers in Q1–Q4 over 4 days of observation. (P) Percentages of blue, red, and green tumor cells in Q1–Q4.

replication was imaged over several days by two-photon microscopy. We are able to obtain, with single-cell resolution, serial and non-invasive imaging of tumor cells expressing a fluorescent protein and replication therein of a MV expressing a different fluorophore. We compared replication and oncolysis of a fusogenic and a hypofusogenic MV, and we observed distinctly different replication kinetics and phenotypes of these two viruses. Information gained from these *in vivo* high-resolution imaging studies can be used to further understand and optimize MV oncolytic virotherapy.

RESULTS

Serial Intravital Imaging of Multicolored HT1080 Tumor Cells

To capture the dynamics of individual tumor cells at a single-cell resolution, human fibrosarcoma (HT1080) cells were generated that stably express tdTomato, EGFP, or EBFP2, containing an NLS that allows for easy quantification of cells (HT1080-tdTomato-NLS,

HT1080-EGFP-NLS, and HT1080-EBFP-NLS). HT1080 cells have been shown to grow well in the DSFC, the imaging model used in this study,[20] and to support MV replication.[25] Orthotopic tumors consisting of a mixture of the three colored HT1080 cell lines were grown dorsally in athymic NCRNU mice. Once tumors reached a size of 80–300 mm^3, the DSFC was implanted over the tumor (Figure 1A). To image the same area over multiple days, a gridded coverslip was inserted and its numbers were visualized by reflectance imaging (Figure 1B). The tumor was imaged with a two-photon microscope on 4 consecutive days (Figures 1C–1F). Although the lens used in this study has a working distance (2 mm) needed for imaging deep into tissue, only tumor cells in the vicinity of the coverslip were accessible for imaging.

Quantification of the z stack with the Imaris spot detection software, an internal algorithm that automatically detects point-like structures,

showed that the number of cells in the imaged tumor volume fluctuated over time, with a minimum of 7,486 cells and a maximum of 9,446 cells (Figures 1G–1J). Although the tdTomato-, EGFP-, or EBFP-expressing cell lines were injected at equal ratios, the green cells constituted only a minor population within the established tumor. Single-slice and xz and yz orthogonal views illustrated that small clusters of GFP-expressing cells in the xy, xz, and yz dimensions could be used as coordinates to repeatedly orient the tumor (white circles in Figures 1K–1N). These three reference points were utilized to superimpose four quadrants of equal volume (150 × 150 × 130 μm) at identical positions over 4 days of analysis (Q1–Q4 in Figures 1C–1F), and the numbers of red, green, and blue cells were evaluated. The total number of cells varied between quadrants and changed over time, with a peak at day 2 in all quadrants (Figure 1O). Dynamic changes within the tumor could be seen when the relative composition of the three colors was compared between days. In Q2, Q3, and Q4, HT1080-tdTomato-NLS cells were the predominant cell population. The percentage of HT1080-EBFP-NLS cells increased in all four quadrants over time, whereas the number of HT1080-tdTomato-NLS and HT1080-EGFP-NLS cells decreased (Figure 1P). This result illustrates the substantial cell turnover that occurs within a tumor.

We addressed the apparent inequality in cell color composition of the tumor studied above, and we analyzed the cell composition of different quadrants in the same tumor over time (Figure S1). In all quadrants, HT1080-EBFP-NLS cells were the predominant population, and, in two quadrants, 20% of the tumor consisted of HT1080-EGFP-NLS cells. In a different experiment, the tumors encompassed all three colors in more or less equal fractions (Figure S2). This shows that the color composition of the tumor xenograft is purely based on chance.

Intravital Imaging of MV-EBFP-NLS-Infected Tumor Cells with Single-Cell Resolution

To visualize and quantitate the spread of an oncolytic MV in a population of tumor cells at a single-cell resolution, human fibrosarcoma (HT1080) cells stably expressing either tdTomato or EGFP (HT1080-tdTomato or HT1080-EGFP) were generated. A replication-competent MV based on the Edmonston vaccine strain, which has potent and selective oncolytic activity against a wide range of tumors,[26,27] was engineered to express EBFP2 containing a NLS (Figure 2A). This allows for easy detection and quantification of infected cells. The replication dynamics of this fusogenic virus were compared to the dynamics of a hypofusogenic variant due to a mutation (I98A) in the fusion activation segment of the H gene (MV-I98A-EBFP-NLS[28]). Orthotopic HT1080-tdTomato tumors were grown dorsally in athymic NCRNU mice, and the DSFC was implanted over the tumor. MV-EBFP-NLS virus (3.2 × 10^5 median tissue culture infective dose [TCID$_{50}$]) was injected into the tumor, and viral replication was monitored by intravital imaging with a two-photon microscope.

As seen in Figure 2B, 3 days post-infection the wild-type MV (blue) had infected large areas (volume) of the tumor (red). Quantification

of the z stack with the Imaris spot detection software identified 708 infected cells (Figure 2C). We calculated the fraction of infected cells in the imaged tumor volume. It was determined that a volume of 150 × 150 × 130 μm, which was one quadrant analyzed in Figure 1, contained about 800 cells (Figure 1O). Therefore, we estimated that the volume analyzed in Figure 2 (512 × 512 × 130 μm) contained 9,300 cells and the 708 infected cells (Figure 2C) constituted 7.6% of the imaged tumor volume. To gain further quantitative information on the infected cells, the distances between infected nuclei were determined with the Spots to Spots Closest Distance XTension program (Figure 2D). The radius and color of the spheres reflected the distance to the nearest neighboring cell. The bigger the radius was the greater the distance was to the closest spot. The average minimum distance of the 708 infected cells was 11.98 μm, which was similar to the average minimum distance between uninfected tumor cells (11.35 μm; Figure S3). This suggests that infection was due to the spread of the virus between adjacent cells.

Intravital Imaging of the Replication of the Fusogenic MV-EBFP-NLS Virus in HT1080-tdTomato Tumors

We investigated the replication dynamics of the MV-EBFP-NLS virus in HT1080-tdTomato tumors by imaging the same infected tumor area on consecutive days. Figures 3A–3C show the results in the maximum-intensity projection (MIP) mode, which displays the voxels with the maximum intensity of all z sections along the viewing plane. As early as 1 day post-infection (dpi) of the virus, infected tumor cells were visible (Figure 3A). The same tumor area was imaged again 24 h later (Figure 3B), and a rapid spread of the infection was observed, from 55 infected cells (1.7% of imaged tumor volume) at 1 dpi (Figure 3D) to 818 cells (19% of imaged tumor volume) at 2 dpi (Figure 3E). At 3 dpi, many cells were dying and a large area of the tumor was destroyed (Figure 3C), which was reflected in a decrease in the number of infected cells to 614 (Figure 3F). At 4 dpi, no tumor cells were seen in the area of interest (data not shown).

The Spots to Spots Closest Distance analysis revealed that the average minimum distance between infected nuclei was highest at 1 dpi (30.4 μm), when only a few cells were infected (Figure 3G), and decreased to 11.2 μm at 2 dpi (Figure 3H) and to 12.1 μm at 3 dpi (Figure 3I). The average minimum distance of 30.4 μm at 1 dpi also suggested that, at the time of initial administration of the virus, distinct foci of infection developed due to independent infection of single cells. This experiment, together with others not shown, demonstrates that a fusogenic MV spreads rapidly through a tumor, with peak infection 2 days after virus administration (see also Figure 6A).

Intravital Imaging of the Replication of the Hypofusogenic MV-I98A-EBFP-NLS Virus

Mathematical modeling has suggested that oncolytic viruses that lead to slower cell death may ultimately result in better disease control.[29,30] Therefore, we generated a hypofusogenic MV-I98A-EBFP-NLS virus, where isoleucine at position 98 in the hemagglutinin (HA) gene is replaced by an alanine (Figure 2A). This virus has normal receptor
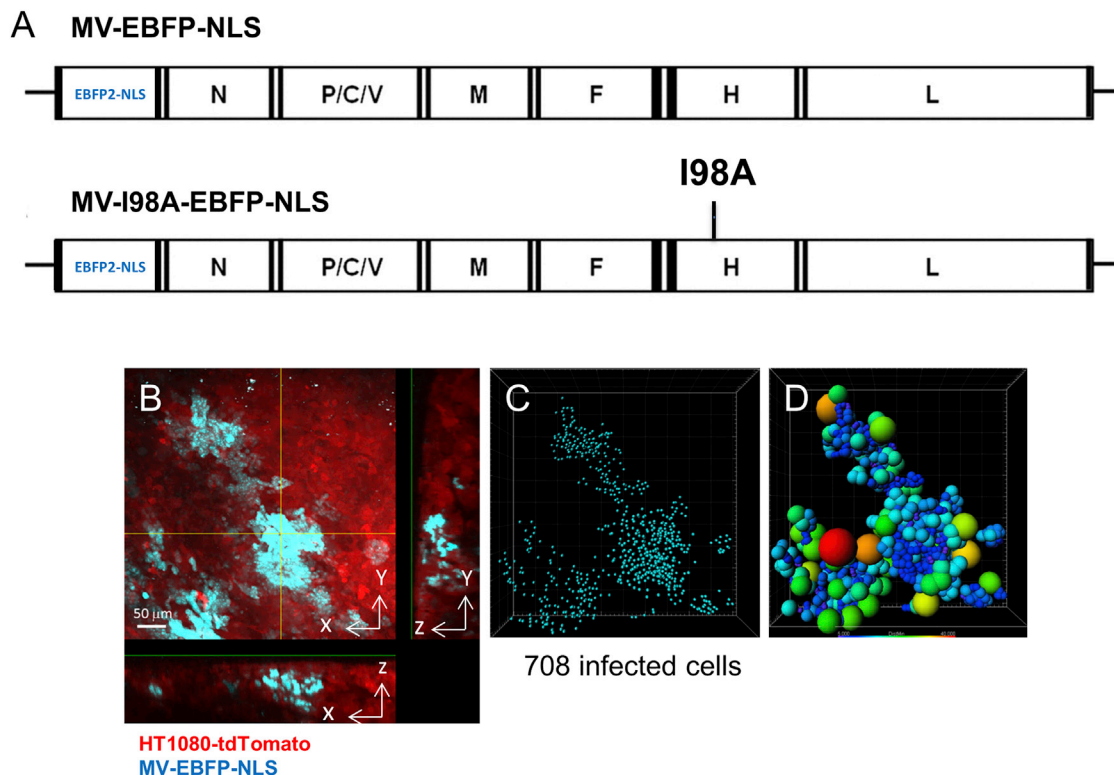
Figure 2. Intravital Imaging of MV-EBFP-NLS-Infected Tumor Cells with Single-Cell Resolution

(A) Schematic representation of the plasmids coding for the measles virus (MV)-EBFP-NLS (fusogenic) and MV-I98A-EBFP-NLS (hypofusogenic) measles virus genomes. The EBFP2 gene containing an NLS was placed upstream of the N gene. The isoleucine at position 98 in the hemagglutinin gene was replaced by an alanine, which makes this virus hypofusogenic.[28] (B) Maximum-intensity projection (MIP) and xz and yz orthogonal views of an HT1080-tdTomato tumor (red) grown in the DSFC and infected with MV-EBFP-NLS (blue nuclei). A 152-μm z stack was acquired 3 days post-infection. Scale bar, 50 μm. (C) The number of infected cells was determined by counting blue nuclei with the Imaris spot analysis software. (D) The distance of each spot to its nearest neighbor was determined with the Spots to Spots Closest Distance XTension program. The radius and color of the spheres reflect the distance to the most proximal neighbor cell. The bigger the radius is the greater the distance is from another spot.

binding, but it infects cells at a lower rate than the wild-type virus due to a reduction in fusion triggering.[28] A tumor consisting of both HT1080-tdTomato and HT1080-GFP cells was infected with this hypofusogenic virus (5.3×10^5 TCID$_{50}$) in the DSFC. Figure 4 shows overlapping maximum-intensity projections of the same infected tumor area (volume) imaged on consecutive days.

The earliest time point when MV-I98A-EBFP-NLS-infected cells (magenta) were visible was 3 days post-infection (Figure 4A). In other similar experiments, infected cells were visible only as early as 5 dpi (data not shown), which is in stark contrast to the wild-type virus. The infection was spreading over the next 2 days (Figures 4B and 4C) and reached its maximum at 6 dpi (Figure 4D), at which time point some tumor tissue was already destroyed (see arrow in Figure 4D, lower panel). By 7 dpi, vast areas of the tumor were eradicated. It is thought that oncolytic MVs kill cells by inducing cell-to-cell fusion and the formation of giant cell syncytia that ultimately die.[3] However, it has been quite difficult to observe multinucleated syncytia *in vivo* within tumor xenografts infected with recombinant MV. Figure 4F shows an individual 2D slice and xz and yz orthogonal views of a z stack of the outlined area in Figure 4A. A multinucleated syncytium, containing 186 nuclei, is delineated with a white dotted line, demonstrating that even the hypofusogenic MV-I98A-EBFP-NLS virus is capable of forming large syncytia *in vivo*. When the green channel (HT1080-EGFP) and the red channel (HT1080-tdTomato) were analyzed individually, we determined that green and red cells were fused and are present in the syncytium (Figures S4A–S4C). This was corroborated by a fluorescence intensity profile across the tumor including the syncytium, which confirmed that both red and green cells contributed to the formation of the syncytium (Figures S4D and S4E). Syncytia were also seen with the fusogenic virus (Figure S5).

Quantification of MV-I98A-EBFP-NLS-Infected Cells

To quantitate the replication dynamics of the hypofusogenic virus, the number of infected cells was determined in three tumor regions (Figure 5A, white boxes labeled a, b, and c; z dimension, 100 μm), which were easy to locate on consecutive imaging days, due to their
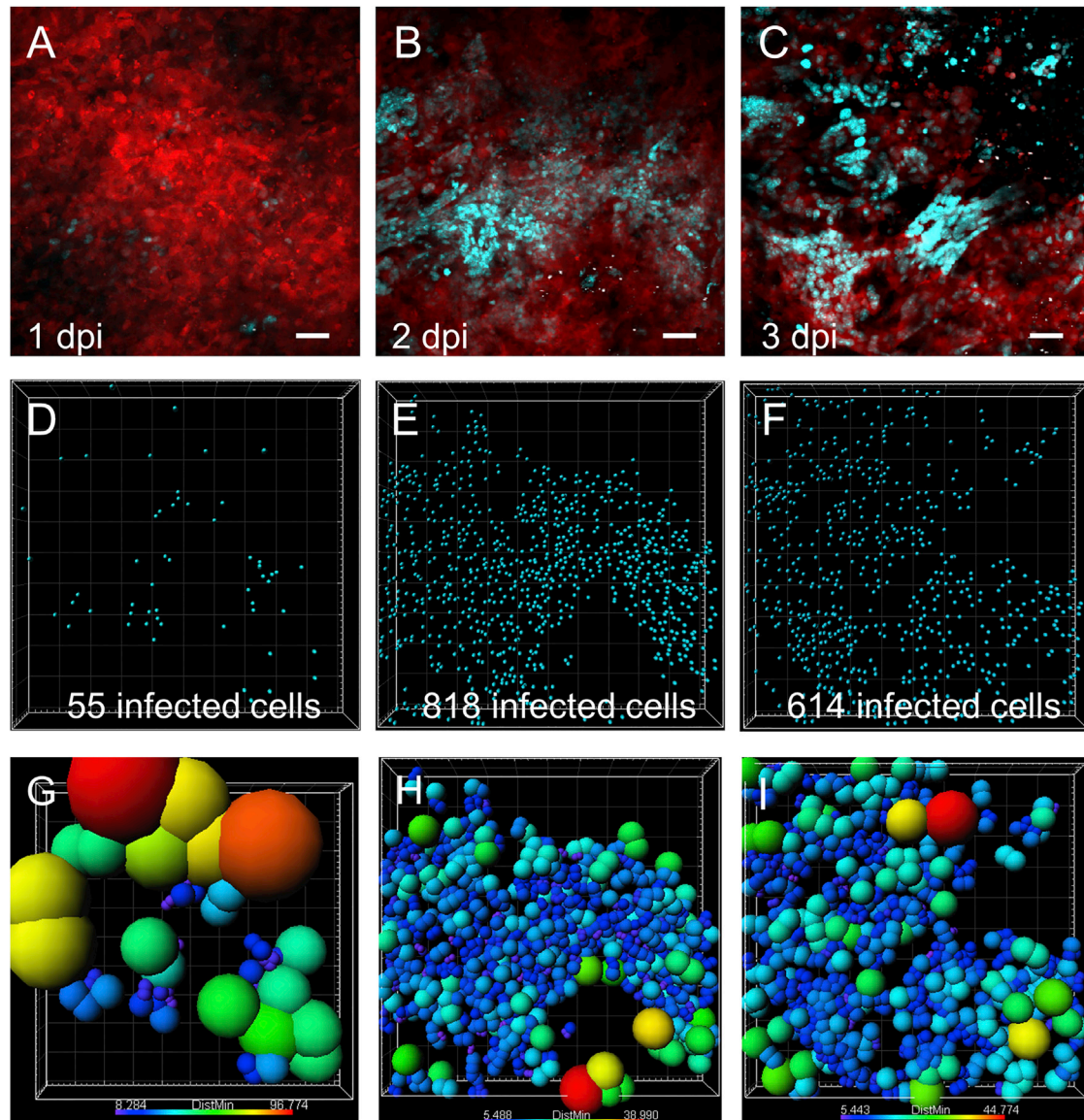
Figure 3. Intravital Imaging of the Replication of the Fusogenic MV-EBFP-NLS Virus in HT1080-tdTomato Tumor

(A–C) Maximum-intensity projections of HT1080-tdTomato tumors (red) grown in the DSFC and infected with MV-EBFP-NLS (blue nuclei), imaged at day 1 (A), day 2 (B), or day 3 post-infection (C). Scale bars, 50 μm. (D–F) The number of infected cells was determined at 1 dpi (D), 2 dpi (E), and 3 dpi (F) with the Imaris spot analysis software. (G–I) Illustration of the distances to the closest neighbor for each spot at 1 dpi (G), 2 dpi (H), and 3 dpi (I).

proximity to blood vessels. The virus displayed different dynamics in the three areas analyzed. The least number of infected cells was observed in area a, where the infection peaked at 5 dpi with 131 infected cells. In contrast, in areas b and c, the peak of infection was reached only at day 6 with 217 and 353 infected cells, respectively. The most dramatic change occurred in area c, where the number of infected cells increased almost 4-fold between 5 and 6 dpi. Similar infection dynamics were observed when a different region of the same tumor was analyzed (Figures S6 and S7). The opposite was seen when the minimum distances between nuclei

of infected cells were measured. In the above example (area c), the median of the minimum distances decreased from 18.9 μm at 5 dpi to 10.7 μm at 6 dpi, which was similar to the minimum distance of nuclei in uninfected tumor cells (10.94 μm, data not shown). This also suggests that the virus was spreading from cell to cell, with adjacent cells at the highest risk of infection. However, it is important to note that some tumor areas remained uninfected during the 7 days of imaging, although they were consistently in close proximity to infected cells (area with asterisk in Figures 5A–5E).
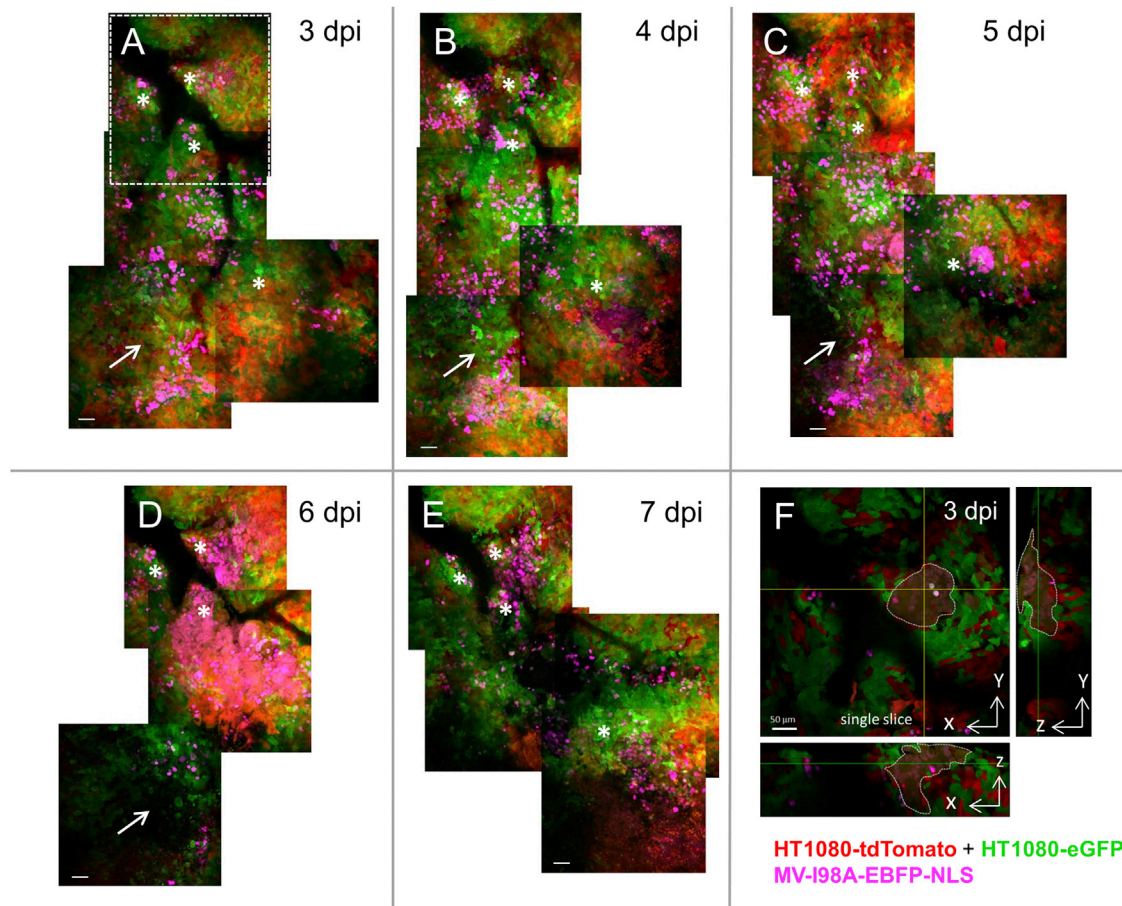
Figure 4. Intravital Imaging of the Replication of the Hypofusogenic MV-I98A-EBFP-NLS Virus

(A–E) Overlapping maximum-intensity projections of tumors consisting of HT1080-tdTomato and HT1080-EGFP cells infected with MV-I98A-EBFP-NLS (magenta), imaged at 3 dpi (A), 4 dpi (B), 5 dpi (C), 6 dpi (D), and 7 dpi (E). (F) Individual 2D slice and xz and yz orthogonal views of a z stack of the outlined area in (A). A multinucleated syncytium is outlined with a white dotted line. Scale bars, 50 μm.

Kinetics of Viral Spread

To quantitate the kinetics of viral spread, we determined the average number of infected cells for each day post-infection from all experiments performed. The analysis includes 27 tumor foci from 8 mice infected with MV-wild-type (WT) and 49 tumor foci from 3 mice infected with MV-I98A. As seen in Figure 6A and Figure S8, the wild-type and the mutant virus exhibited clear differences. The fusogenic (MV-EBFP-NLS) virus peaked early, around day 2 post-infection, and killed tumor cells quickly. In contrast, the hypofusogenic virus (MV-I98A-EBFP-NLS) on average spread at a slower rate, and the infected cell population reached a peak around 6 dpi. The area under the curve for each virus was also substantially different: 2,106 infected cell days versus 686 infected cell days for MV-EBFP-NLS and MV-I98A-EBFP-NLS, respectively. These differences were also reflected in the number of infected cells per focus (Figure 6B) and the median of the minimum distances between infected nuclei (Figure 6C). We see a statistically significant difference between the two viruses, with the fusogenic one containing on average 460 infected cells per focus, whereas the hypofusogenic virus had only 126 cells per focus. The average of the median of the minimum distances between infected cells was significantly lower for the wild-type virus (12.52 μm) than for the mutant virus (15.22 μm).

DISCUSSION

In the last decade, significant progress has been made in the understanding and treatment of cancer, and many novel therapeutics, including small molecules, monoclonal antibodies, and now oncolytic viruses, are available. The field of oncolytic virotherapy is advancing by genetically modifying viruses for the selective infection and destruction of cancer cells. Viruses from nine different families are currently undergoing clinical trials, one of them being the MV.[1,2] MV-NIS is a live attenuated virus, derived from the Edmonston vaccine strain, engineered to express the sodium iodide symporter.[5] This modification not only enables *in vivo* imaging of the location of the virus but also potentially enhances its oncolytic activity when combined with beta-emitting isotopes, such as [131]I.[5]
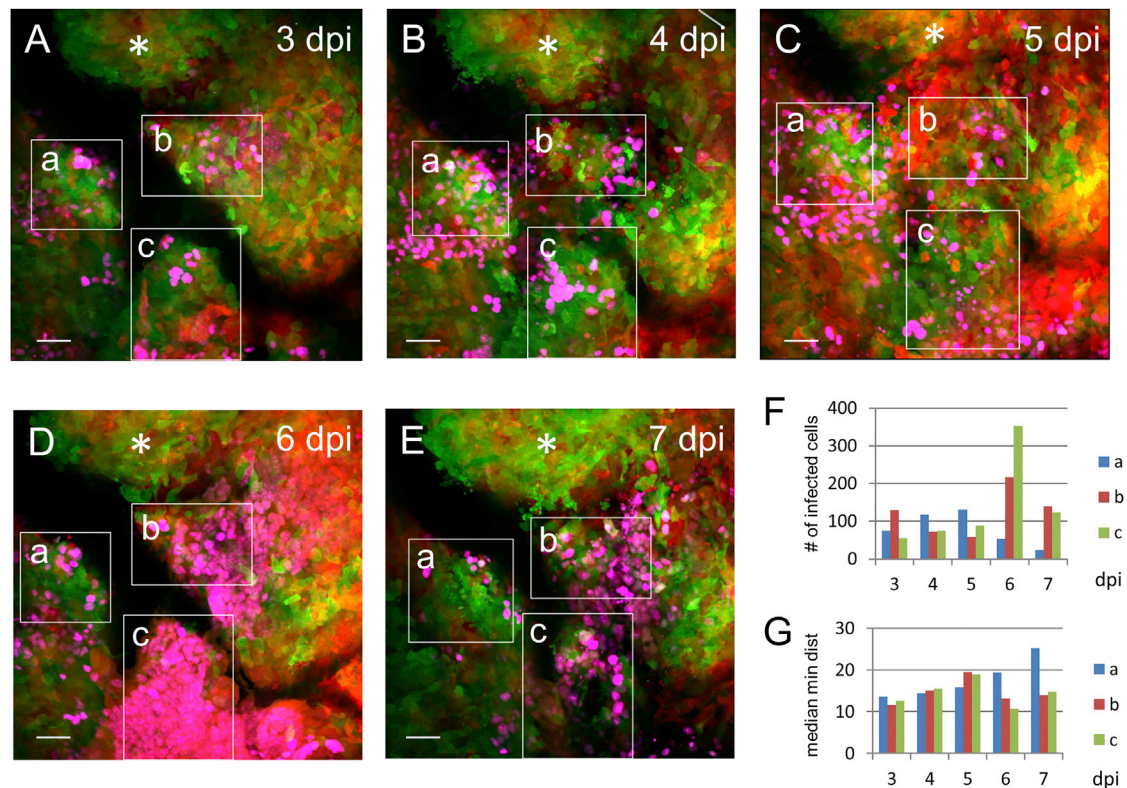
Figure 5. Quantification of MV-I98A-EBFP-NLS-Infected Cells

(A–E) The Imaris spot analysis software was used to detect infected nuclei in three regions of interest (ROIs) (a, b, and c), in the area outlined in Figure 4A, which could be precisely retraced over time at 3 dpi (A), 4 dpi (B), 5 dpi (C), 6 dpi (D), and 7 dpi (E). White asterisks denote uninfected tumor areas. Scale bars, 50 µm. (F and G) Histogram of number of infected cells (F) and median of minimum distances to closest neighbor (G) over time in ROIs.

Recently, as a proof of principle, MV-NIS was shown to lead to long-term disease control for a disseminated malignancy when one patient with relapsed and refractory multiple myeloma experienced meaningful tumor cytoreduction after a single dose of MV-NIS, and the patient remains in remission more than 5 years after virus administration.[6] However, the outcomes of tumor control have been variable in animal models[27] and human studies.[7] An important component for the improvement of oncolytic virotherapy is the ability to understand and document the mechanisms leading to cell killing, e.g., virus replication and spread in the tumor. Documentation of MV spread has been achieved by engineering the virus to express the NIS gene, which allows noninvasive tracking of virus replication in animal models and patients by microCT/SPECT[5,6] or positron emission tomography [PET].[31] However, the resolution of these imaging modalities is currently limited to 0.25 mm.[32] In this paper, we report, with intravital imaging, the cell-to-cell spread of an oncolytic MV within a tumor at an unprecedented single-cell resolution. We accomplished this by combining two-photon microscopy, which can resolve subcellular structures, with the imaging of a virally encoded fluorophore containing an NLS (EBFP-NLS). Expression of the marker protein within infected cells is exclusively intranuclear, enabling high-resolution quantitation of the number of infected cells. By performing those im-

aging studies in a DSFC in a live animal, we were able to study tumor cell dynamics and viral replication in four dimensions.

Here we compare the replication dynamics of a fusogenic MV (MV-EBFP-NLS) with those of a hypofusogenic MV (MV-I98A-EBFP-NLS) and find distinct differences. The fusogenic virus spreads very fast with a peak of infection at 2–3 days (Figure 3), whereas, with the hypofusogenic virus, the infected tumor cell population reaches a maximum around 6 dpi (Figures 4 and 5). We are unable to say if the observed differences in virus replication kinetics are reflected in tumor clearance. In this experimental system, the tumor burden cannot be determined accurately, since the animals have the DSFC implanted and caliper measurements of the tumors are impossible to perform. Also, measuring change in tumor burden was not a goal of this study.

The two viruses also differ in the size of their infection foci, with the fusogenic one comprising on average 3.6 times more infected cells per focus than the hypofusogenic virus (Figure 6). This can be explained by the fact that the I98A mutation in the MV hemagglutinin protein is situated in the central fusion-activating segment spanning residues 84–117.[33] The mutant virus binds to its receptor normally, but
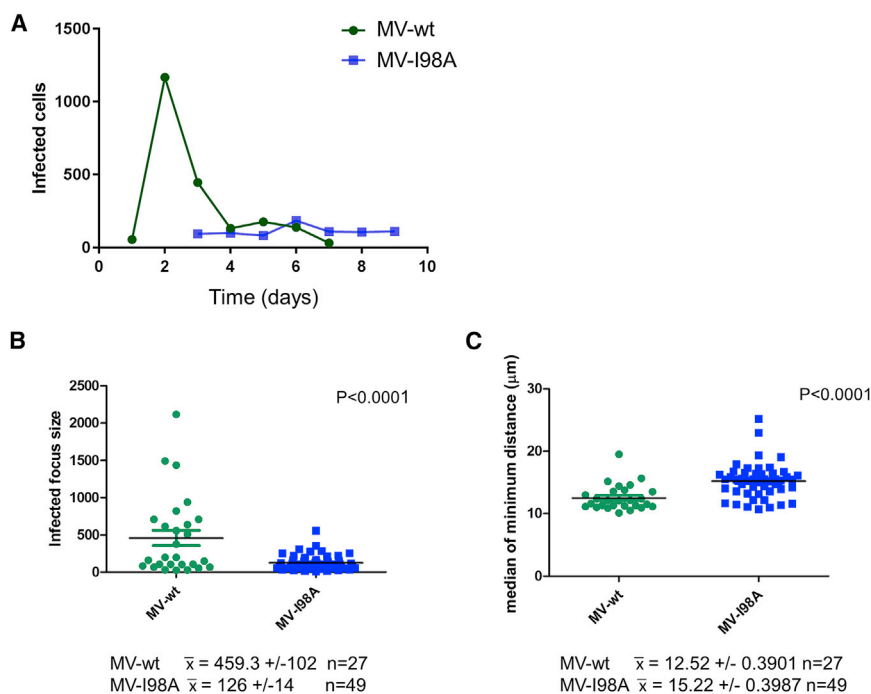
Figure 6. Kinetics of Viral Spread

(A) Average numbers of cells infected with MV-EBFP-NLS (WT, green) and MV-I98A-EBFP-NLS (I98A, blue) for each day post-infection. (B) Comparison of size of infection foci between WT and I98A virus. (C) Comparison of the median of the minimum distances to the closest neighbor of infected cells between WT and I98A virus.

MV-wt $\bar{x}$ = 459.3 +/-102   n=27
MV-I98A $\bar{x}$ = 126 +/-14   n=49

MV-wt $\bar{x}$ = 12.52 +/- 0.3901 n=27
MV-I98A $\bar{x}$ = 15.22 +/- 0.3987 n=49

The therapeutic efficacy of oncolytic MV can be enhanced by arming the virus with a therapeutic transgene like a prodrug convertase,[34,35] a radiosensitizer like NIS,[5,32] or an immunostimulatory gene[36] that results in killing of tumor cells that escaped viral infection. It is conceivable that, if those proteins are expressed from a hypofusogenic, slower replicating virus, they last longer in the tumor and have more time to act on non-infected tumor cells, and, therefore, the therapeutic outcome in such a scenario could be better for a slower virus.

Since the virus infects a small number of cells initially (cf. Figure 3A), one can assume that each syncytium is likely the result of a single-cell infection that amplifies the virus and that spreads locally either by the induction of cell-to-cell fusion or release of virus that infects cells in close proximity. The number of infected cells, therefore, gives a measure of the amplification of the virus that occurs within the tumor. This is a distinct feature of tumor virotherapy, where the target of therapy itself amplifies the therapeutic agent. In contrast, virtually every other form of therapy is eliminated during tumor cell killing due to metabolism (the only obvious other exception is CAR-T cell therapy).

infection is delayed because the fusion-triggering function is impaired. Nevertheless, the mutant virus forms large multinucleated syncytia in vivo (Figure 4F) and is very efficient in tumor cell killing. Is a slowly replicating virus a better oncolytic virus? Mathematical modeling suggested that weakly cytopathic viruses may provide more tumor cytoreduction than viruses that destroy cells rapidly,[29] since this will lead to higher virus amplification and, therefore, potentially more infected cells. However, our finding that the fusogenic MV forms much larger infection foci and has a larger area under the curve for therapy, and, therefore, kills more cells than the hypofusogenic MV, would argue against this. Moreover, given that the immune response will likely neutralize the virus and halt further spread of the oncolytic, perhaps faster virus replication and cell killing will end up being a better approach. However, the current technology does not allow us to study the influence of the immune system on MV replication and oncolysis.

One limitation of our work is that the in vivo experiments were in immunocompromised animals, and we cannot study the impact of the immune system on virus spread. However, the xenograft model used in this imaging study is similar to the models used for preclinical testing of the antitumor effect of oncolytic MV. However, we cannot exclude that, in an immunocompetent host, tumor-infiltrating immune cells could not have an effect on the spread of the virus. It would be interesting to apply this intravital imaging modality to an immunocompetent mouse model where the virus is retargeted to a mouse cell expressing the corresponding receptor.[27] Nevertheless, such a system is also not ideal, because, although the MV can be retargeted to enter murine cells, replication in such cells is suboptimal since MV replication in murine cells is restricted by host factors.

The amount and quality of information gained from our intravital two-photon imaging system is superior to SPECT imaging, as demonstrated in Figure 5 where the infected tumor area would be considered one single infection focus with SPECT/computed tomography (CT) imaging. However, our analysis clearly shows that this area is composed of several distinct micro-foci and the virus replicates in each focus with different kinetics. In sub-region a, the virus spreads slowly between 3 and 5 dpi and then declines, whereas in area c the number of infected cells increases almost 4-fold between days 5 and 6. This should be taken into consideration when trying to understand virotherapy with mathematical modeling. In those models it is often assumed that the infection centers expand radially at the same speed.[37,38] However, as seen in Figure 4F, an infection can spread asymmetrically. We observed that some parts of the tumor were not infected during the 7 days of imaging, although they were in close proximity to infected cells (area with asterisk in Figures 5A–5E). Similarly, Miest et al.[39] reported regions of perfused, viable tumor (mantle cell lymphoma) that were not infected by an oncolytic MV-NIS. Miller et al.[40] described intratumoral infection voids after the administration of a vesicular stromatitis virus (VSV)-derived oncolytic

virus. However, the latter study did not address whether the uninfected areas consisted of viable tumor cells or necrotic tissue. Clearly, the spatial relationships between cells can have a major influence on the outcome of therapy with such oncolytic viruses. Significant anisotropies in the distribution and rate of spread of infection within the same tumor exist, and these together with the impact of the tumor architecture on the dynamics of spread of these viruses need to be understood for optimal tumor control.

The median of the minimum distances between nuclei of infected cells is statistically different between the wild-type (12.52 μm) and the I98A virus (15.22 μm; see Figure 6C). This sheds insights into the rate of spread of the viruses: while the wild-type virus infects cells rapidly and the minimum distance approaches that of normal cells, the hypofusogenic virus infects at a slower rate and, therefore, the distance between infected cells is on average larger. In the rare events where the I98A virus infected a larger area (Figure 5D, box c), the median minimum distance between nuclei was smaller, 10.71 μm, comparable to the distance between nuclei in uninfected tumors (11.35 μm).

Since tumors arise due to the accumulation of mutations, mostly during DNA replication, it is important to capture the replication dynamics of tumor cells. Uniformly labeled tumors provide a macroscopic view of the population, but subtle changes involving only a few cells are not discernible. Here we imaged tumors consisting of three different colors (red, green, and blue) over consecutive days in a live animal. This model system is designed to investigate cell turnover within the tumor, not clonal dynamics or tumor population growth. Quantitative analysis of each colored cell population in a defined volume revealed significant changes within the 3 subpopulation fractions that constituted the tumor (Figure 1). These observations imply that there is more cell turnover within the tumor than what a single macroscopic measure of total population growth would suggest. These changes may play an important role in tumor evolution, since the effective number of cell replications will be higher per unit of time.

In summary, we have established an intravital imaging system using the DSFC and two-photon microscopy, which allows us to image the replication of a MV *in vivo* in tumors over time at a single-cell resolution. We compared the replication and oncolysis of a fusogenic and a hypofusogenic MV, and we observed distinctly different replication kinetics and phenotypes. The fusogenic virus spreads and kills cells rapidly. However, barriers to virus spread remain that limit its access to areas of the tumor and, therefore, have an impact on the outcome of therapy. Inexplicably, some tumor areas adjacent to a rapidly expanding focus of infection remain uninfected and will lead to the failure of therapy. This system can be adapted to other preclinical models, using different cell lines and viruses, including immunocompetent mouse models in which the influence of the immune system on tumor oncolysis could be investigated. Further, we believe that information gained from *in vivo* imaging can be used to develop, optimize, and test predictive computational algorithms for the best use of oncolytic virotherapy.

MATERIALS AND METHODS

Cells

To generate the cell lines HT1080-tdTomato, HT1080-EGFP, HT1080-tdTomato-NLS, HT1080-EGFP-NLS, and HT1080-EBFP-NLS, the parental line HT1080 (human fibrosarcoma) was transduced with lentiviral particles encoding the tdTomato, EGFP, tdTomoto-NLS, EGFP-NLS, or EBFP2-NLS genes,[41] respectively. Single-cell clones were obtained by limiting dilution. Cell lines were grown in DMEM supplemented with 10% fetal bovine serum and 1% penicillin and streptomycin at 37°C in a humidified atmosphere of 5% CO_2.

Viruses

The MV-EBFP-NLS plasmid was generated by replacing GFP upstream of the N transcription unit in the plasmid p(+)MV-EGFP,[28] with EBFP2 containing an NLS. EBFP2-NLS was amplified by PCR from pEBFP2-Nuc (Addgene 14893) with the following primers, where the restriction sites are underlined: MV-EBFP-MluI-fwd, 5′-GACGCGTACGCCACCATGGTGAGCAAGGGCGAGG-3′; and MV-EBFPNLS-AatII-rev, 5′-CGAGACGTCAGTTTATTATCTAGA TCCGGTGGATCCTACC-3′. The digested PCR product was cloned into p(+)MV-EGFP digested with MluI and AatII. MV-I98A-EBFP-NLS was generated by replacing a 1,937-bp PacI and SpeI restriction fragment containing the H gene with a corresponding fragment excised from the MV-I98A plasmid where the isoleucine at position 98 is replaced by an alanine.[28] Recombinant viruses were generated as described previously.[42] Titers were determined on Vero cells.

Animal Studies

All procedures and animal protocols were approved by the Mayo Institutional Animal Care and Use committee. The 4- to 6-week-old female athymic nude mice (strain NCRNU) were purchased from Taconic (Hudson, NY). The mice were allowed 1 week to acclimate before any experiments.

Implantation of the Dorsal Skin Fold Chamber

10^6 HT1080-tdTomato and HT1080-EGFP cells (1:1) in PBS were injected subcutaneously into the dorsal skin. Titanium DSFCs (APJ Trading) were implanted 10–12 days later when the tumors reached a size of 80–300 mm³, using previously described methods.[19,43] Mice were anesthetized by intraperitoneal injection of ketamine (100 mg/kg) and xylazine (10 mg/kg), and they were placed on a thermostatic blanket in a laminar flow hood. Before surgery, buprenorphine (0.1 mg/kg) was administered subcutaneously. After disinfecting the back of the mouse with betadine, the dorsal skin was lifted along the centerline and secured to a C-shaped holder. One frame of the window chamber was placed against the skin fold and the positions of the screw holes were marked. With a 16G needle, a hole was punched through both sides of the skin at each of the screw locations. After the front window chamber was positioned and screws were inserted through the three holes, the rear frame was attached and fastened with nuts. The chamber was secured with sutures through the skin and the frames. The C-shaped holder was removed.

The forward-facing portion of the skin was removed within the circular window, and a glass coverslip with a photoetched numerical grid (Bellco 1916-91012) was placed over the tumor and secured with a retaining ring (snap ring). After a day of recovery, the tumors were injected with virus (MV-EBFP-NLS 3.2×10^5 TCID$_{50}$ or MV-I98A-EBFP-NLS 5.3×10^5 TCID$_{50}$) from the side opposite of the glass coverslip using a Hamilton syringe and a 30G needle. The drinking water contained amoxicillin (250 mg/500 mL water).

Intravital Imaging

Mice were anesthetized with 2% isoflurane (v/v) and placed in a customized holder to immobilize the mouse and the DSFC. A heating pad was draped over the holder to prevent murine hypothermia. Intravital imaging was performed on an Olympus Fluoview FW1000 multiphoton microscope equipped with a Mai-Tai DeepSee laser, with a tuning wavelength range from 690 to 1,040 nm. All images (12 bit, 512×512 pixels, Kalman averaging 2) were acquired with a 25× and 1.05 numerical aperture (NA), water immersion objective (Olympus). The z stacks consisted of 1.5-μm slices. EBFP2 and tdTomato were excited simultaneously with 750 nm, taking advantage of the observation that tdTomato is efficiently excited at shorter wavelengths;[44–46] EGFP was excited at 810 nm. Emitted light was separated into three detection channels: 420–460 nm for EBFP2, 495–545 nm for EGFP, and 575–630 nm for tdTomato. To image the same area over multiple days, the grid number corresponding to the area was visualized by reflectance imaging.[47] The tissue in close proximity to the coverslip was excited with a 488-nm wavelength, and the emitted light was detected at 505–605 nm (Figure 1B).

Image Analysis

The number of infected cells was quantitated by counting the number of EBFP2-containing nuclei with the spot detection tool of the Imaris version 8.2.0 (Bitplane) software. This is an internal algorithm that automatically detects point-like structures. The minimum distances between infected nuclei (spots) were calculated with the Imaris Spots to Spots Closest Distance Xtension. All statistical studies were performed using GraphPad Prism version 7 (La Jolla, CA). Comparisons between groups were with the Mann-Whitney test and $p < 0.05$ was considered significant.

SUPPLEMENTAL INFORMATION

Supplemental Information includes eight figures and can be found with this article online at https://doi.org/10.1016/j.omto.2018.12.007.

AUTHOR CONTRIBUTIONS

I.K. and D.D. designed and analyzed the experiments and wrote the manuscript. M.K.E. made the HT1080-tdTomato and HT1080-EGFP cell lines. I.K. performed the experiments. C.M.N. provided advice and made suggestions for the manuscript. All authors edited the paper.

CONFLICTS OF INTEREST

The authors declare no competing interests.

ACKNOWLEDGMENTS

REFERENCES

1. Bell, J., and McFadden, G. (2014). Viruses for tumor therapy. Cell Host Microbe 15, 260–265.

2. Miest, T.S., and Cattaneo, R. (2014). New viruses for cancer therapy: meeting clinical needs. Nat. Rev. Microbiol. 12, 23–34.

3. Peng, K.-W., Donovan, K.A., Schneider, U., Cattaneo, R., Lust, J.A., and Russell, S.J. (2003). Oncolytic measles viruses displaying a single-chain antibody against CD38, a myeloma cell marker. Blood 101, 2557–2562.

4. Russell, S.J., Peng, K.-W., and Bell, J.C. (2012). Oncolytic virotherapy. Nat. Biotechnol. 30, 658–670.

5. Dingli, D., Peng, K.W., Harvey, M.E., Greipp, P.R., O'Connor, M.K., Cattaneo, R., Morris, J.C., and Russell, S.J. (2004). Image-guided radiovirotherapy for multiple myeloma using a recombinant measles virus expressing the thyroidal sodium iodide symporter. Blood 103, 1641–1646.

6. Russell, S.J., Federspiel, M.J., Peng, K.W., Tong, C., Dingli, D., Morice, W.G., Lowe, V., O'Connor, M.K., Kyle, R.A., Leung, N., et al. (2014). Remission of disseminated cancer after systemic oncolytic virotherapy. Mayo Clin. Proc. 89, 926–933.

7. Dispenzieri, A., Tong, C., LaPlant, B., Lacy, M.Q., Laumann, K., Dingli, D., Zhou, Y., Federspiel, M.J., Gertz, M.A., Hayman, S., et al. (2017). Phase I trial of systemic administration of Edmonston strain of measles virus genetically engineered to express the sodium iodide symporter in patients with recurrent or refractory multiple myeloma. Leukemia 31, 2791–2798.

8. Ayala-Breton, C., Russell, L.O.J., Russell, S.J., and Peng, K.-W. (2014). Faster replication and higher expression levels of viral glycoproteins give the vesicular stomatitis virus/measles virus hybrid VSV-FH a growth advantage over measles virus. J. Virol. 88, 8332–8339.

9. Wu, J.T., Kirn, D.H., and Wein, L.M. (2004). Analysis of a three-way race between tumor growth, a replication-competent virus and an immune response. Bull. Math. Biol. 66, 605–625.

10. Wodarz, D. (2013). Computational modeling approaches to studying the dynamics of oncolytic viruses. Math. Biosci. Eng. 10, 939–957.

11. Rommelfanger, D.M., Offord, C.P., Dev, J., Bajzer, Z., Vile, R.G., and Dingli, D. (2012). Dynamics of melanoma tumor therapy with vesicular stomatitis virus: explaining the variability in outcomes using mathematical modeling. Gene Ther. 19, 543–549.

12. Dingli, D., Cascino, M.D., Josić, K., Russell, S.J., and Bajzer, Z. (2006). Mathematical modeling of cancer radiovirotherapy. Math. Biosci. 199, 55–78.

13. Dingli, D., Offord, C., Myers, R., Peng, K.W., Carr, T.W., Josic, K., Russell, S.J., and Bajzer, Z. (2009). Dynamics of multiple myeloma tumor therapy with a recombinant measles virus. Cancer Gene Ther. 16, 873–882.

14. Haddad, D., and Fong, Y. (2015). Molecular imaging of oncolytic viral therapy. Mol. Ther. Oncolytics 1, 14007.

15. Helmchen, F., and Denk, W. (2005). Deep tissue two-photon microscopy. Nat. Methods 2, 932–940.

16. Condeelis, J., and Weissleder, R. (2010). In vivo imaging in cancer. Cold Spring Harb. Perspect. Biol. 2, a003848.

17. Wyckoff, J., Gligorijevic, B., Entenberg, D., Segall, J., and Condeelis, J. (2011). High-resolution multiphoton imaging of tumors in vivo. Cold Spring Harb. Protoc. 2011, 1167–1184.

18. Biesecker, M., Kimn, J.H., Lu, H., Dingli, D., and Bajzer, Z. (2010). Optimization of virotherapy for cancer. Bull. Math. Biol. 72, 469–489.

19. Laschke, M.W., Vollmar, B., and Menger, M.D. (2011). The dorsal skinfold chamber: window into the dynamic interaction of biomaterials with their surrounding host tissue. Eur. Cell. Mater. 22, 147–164, discussion 164–167.

20. Alexander, S., Koehl, G.E., Hirschberg, M., Geissler, E.K., and Friedl, P. (2008). Dynamic imaging of cancer growth and invasion: a modified skin-fold chamber model. Histochem. Cell Biol. 130, 1147–1154.

21. Alieva, M., Ritsma, L., Giedt, R.J., Weissleder, R., and van Rheenen, J. (2014). Imaging windows for long-term intravital imaging: General overview and technical insights. Intravital 3, e29917.

22. Beerling, E., Ritsma, L., Vrisekoop, N., Derksen, P.W.B., and van Rheenen, J. (2011). Intravital microscopy: new insights into metastasis of tumors. J. Cell Sci. 124, 299–310.

23. Baron, V.T., Welsh, J., Abedinpour, P., and Borgström, P. (2011). Intravital microscopy in the mouse dorsal chamber model for the study of solid tumors. Am. J. Cancer Res. 1, 674–686.

24. Borgström, P., Hillan, K.J., Sriramarao, P., and Ferrara, N. (1996). Complete inhibition of angiogenesis and growth of microtumors by anti-vascular endothelial growth factor neutralizing antibody: novel concepts of angiostatic therapy from intravital videomicroscopy. Cancer Res. 56, 4032–4039.

25. Springfeld, C., von Messling, V., Frenzke, M., Ungerechts, G., Buchholz, C.J., and Cattaneo, R. (2006). Oncolytic efficacy and enhanced safety of measles virus activated by tumor-secreted matrix metalloproteinases. Cancer Res. 66, 7694–7700.

26. Msaouel, P., Iankov, I.D., Dispenzieri, A., and Galanis, E. (2012). Attenuated oncolytic measles virus strains as cancer therapeutics. Curr. Pharm. Biotechnol. 13, 1732–1741.

27. Robinson, S., and Galanis, E. (2017). Potential and clinical translation of oncolytic measles viruses. Expert Opin. Biol. Ther. 17, 353–363.

28. Ennis, M.K., Hu, C., Naik, S.K., Hallak, L.K., Peng, K.W., Russell, S.J., and Dingli, D. (2010). Mutations in the stalk region of the measles virus hemagglutinin inhibit syncytium formation but not virus entry. J. Virol. 84, 10913–10917.

29. Bajzer, Z., Carr, T., Josić, K., Russell, S.J., and Dingli, D. (2008). Modeling of cancer virotherapy with recombinant measles viruses. J. Theor. Biol. 252, 109–122.

30. Wodarz, D. (2003). Gene therapy for killing p53-negative cancer cells: use of replicating versus nonreplicating agents. Hum. Gene Ther. 14, 153–159.

31. Dingli, D., Kemp, B.J., O'Connor, M.K., Morris, J.C., Russell, S.J., and Lowe, V.J. (2006). Combined I-124 positron emission tomography/computed tomography imaging of NIS gene expression in animal models of stably transfected and intravenously transfected tumor. Mol. Imaging Biol. 8, 16–23.

32. Miller, A., and Russell, S.J. (2016). The use of the NIS reporter gene for optimizing oncolytic virotherapy. Expert Opin. Biol. Ther. 16, 15–32.

33. Navaratnarajah, C.K., Kumar, S., Generous, A., Apte-Sengupta, S., Mateo, M., and Cattaneo, R. (2014). The measles virus hemagglutinin stalk: structures and functions of the central fusion activation and membrane-proximal segments. J. Virol. 88, 6158–6167.

34. Ungerechts, G., Frenzke, M.E., Yaiw, K.C., Miest, T., Johnston, P.B., and Cattaneo, R. (2010). Mantle cell lymphoma salvage regimen: synergy between a reprogrammed oncolytic virus and two chemotherapeutics. Gene Ther. 17, 1506–1516.

35. Ungerechts, G., Springfeld, C., Frenzke, M.E., Lampe, J., Johnston, P.B., Parker, W.B., Sorscher, E.J., and Cattaneo, R. (2007). Lymphoma chemovirotherapy: CD20-targeted and convertase-armed measles virus can synergize with fludarabine. Cancer Res. 67, 10939–10947.

36. Lichty, B.D., Breitbach, C.J., Stojdl, D.F., and Bell, J.C. (2014). Going viral with cancer immunotherapy. Nat. Rev. Cancer 14, 559–567.

37. Bailey, K., Kirk, A., Naik, S., Nace, R., Steele, M.B., Suksanpaisan, L., Li, X., Federspiel, M.J., Peng, K.W., Kirk, D., and Russell, S.J. (2013). Mathematical model for radial expansion and conflation of intratumoral infectious centers predicts curative oncolytic virotherapy parameters. PLoS ONE 8, e73759.

38. Wodarz, D., Hofacre, A., Lau, J.W., Sun, Z., Fan, H., and Komarova, N.L. (2012). Complex spatial dynamics of oncolytic viruses in vitro: mathematical and experimental approaches. PLoS Comput. Biol. 8, e1002547.

39. Miest, T.S., Frenzke, M., and Cattaneo, R. (2013). Measles virus entry through the signaling lymphocyte activation molecule governs efficacy of mantle cell lymphoma radiovirotherapy. Mol. Ther. 21, 2019–2031.

40. Miller, A., Suksanpaisan, L., Naik, S., Nace, R., Federspiel, M., Peng, K.W., and Russell, S.J. (2014). Reporter gene imaging identifies intratumoral infection voids as a critical barrier to systemic oncolytic virus efficacy. Mol. Ther. Oncolytics 1, 14005.

41. Dingli, D., Diaz, R.M., Bergert, E.R., O'Connor, M.K., Morris, J.C., and Russell, S.J. (2003). Genetically targeted radiotherapy for multiple myeloma. Blood 102, 489–496.

42. Radecke, F., Spielhofer, P., Schneider, H., Kaelin, K., Huber, M., Dötsch, C., Christiansen, G., and Billeter, M.A. (1995). Rescue of measles viruses from cloned DNA. EMBO J. 14, 5773–5784.

43. Palmer, G.M., Fontanella, A.N., Shan, S., Hanna, G., Zhang, G., Fraser, C.L., and Dewhirst, M.W. (2011). In vivo optical molecular imaging and analysis in mice using dorsal window chamber models applied to hypoxia, vasculature and fluorescent reporters. Nat. Protoc. 6, 1355–1366.

44. Salomonnson, E., Mihalko, L.A., Verkhusha, V.V., Luker, K.E., and Luker, G.D. (2012). Cell-based and in vivo spectral analysis of fluorescent proteins for multiphoton microscopy. J. Biomed. Opt. 17, 96001.

45. Drobizhev, M., Makarov, N.S., Tillo, S.E., Hughes, T.E., and Rebane, A. (2011). Two-photon absorption properties of fluorescent proteins. Nat. Methods 8, 393–399.

46. Tillo, S.E., Hughes, T.E., Makarov, N.S., Rebane, A., and Drobizhev, M. (2010). A new approach to dual-color two-photon microscopy with fluorescent proteins. BMC Biotechnol. 10, 6.

47. Ritsma, L., Steller, E.J., Ellenbroek, S.I., Kranenburg, O., Borel Rinkes, I.H., and van Rheenen, J. (2013). Surgical implantation of an abdominal imaging window for intravital microscopy. Nat. Protoc. 8, 583–594.